ECS Transactions, 85 (8) 151-162 (2018)
10.1149/08508.0151ecst ©The Electrochemical Society

System-on-Chip Sensor Integration in Advanced CMOS Technology

Lado Filipovic and Ayoub Lahlalia
Institute for Microelectronics, Technische Universität Wien, Vienna, Austria

The growing demand for the integration of several functionalities on a single device has peaked with the rise of the Internet of Things. We are technologically near to having sensors in portable and wearable technologies, a feat made possible by the integration of sensor fabrication with CMOS manufacturing. In this paper we address semiconductor metal oxide sensors, which have the potential of becoming a universal sensor. We describe recent capabilities to model relevant materials and processes for these emerging devices and present optimized designs based on those analysis. In this review we discuss the modeling of sensor fabrication, followed by electro-thermo-mechanical analyses, which are essential to estimating stress build-up and sensor lifetimes. We further address the recent advances in understanding the metal oxide layer, which can be treated similarly to a semiconductor transistor, where ionosorption of gas ions creates a surface potential, changing the conducting behavior of the thin film.

Introduction

While aggressive device scaling has taken the front stage in the semiconductor industry for many decades, there is currently an ever-increasing demand for functional integration in a single device. This means not only the integration of an increasing number of transistors along the path of Moore's law, but also the integration of multiple applications on a single device. The rise of the Internet of Things and the Internet of Everything are clear indicators of this trend. The first attempt at this integration dealt with connecting different dies with different functionalities using bonding wires. This method, however, can negatively impact performance and power dissipation, since long wires result in high RC delay and increased circuit resistance, limiting high frequency performance and reducing the device lifetime. The highest efficiency is reached when all functionalities are fabricated on a single substrate – deemed System-on-Chip (SoC). The use of silicon as a substrate material allows for the efficient integration of Microelectromechanical systems (MEMS) and complementary metal oxide semiconductor (CMOS) structures into a truly monolithic device. This is highly challenging, since the typical high temperature associated with sensor fabrication has a negative influence on front end of line (FEOL) devices and back end of line (BEOL) metallization.

In this review we discuss the integration of MEMS gas sensors within an advanced CMOS technology, for which all fabrication steps, required for the sensor fabrication, are below 450°C. The discussion is split into three main sections. The first one introduces semiconductor metal oxide (SMO) sensors and their composition, while the second looks at the design of the microheater element, an essential component of the SMO gas sensor. The final discussion looks at the modeling and simulation capabilities which have been developed in order to better analyze the structure. This type of in-depth analysis has enabled a significant improvement in the design and power optimization of advanced sensors and microheaters: two recent designs are presented and analyzed in this review.

Semiconductor Metal Oxide Sensors

The semiconducting metal oxide sensor is on its way to becoming a universal sensor, since it can be used for many emerging applications in sensor networks, medical applications, food quality monitoring, and wearable devices. At the same time, the thin SMO film can detect a variety of gases, essential to measuring indoor and outdoor air pollution and toxicity in our environment, aspects essential to our global health and safety. The discoveries which enabled the integration of thin SMO films within a CMOS fabrication sequence have opened up a world of possibilities for sensors integrated in electronic components and a broad integration of sensors in our daily lives, which is already packed with electronic components and devices. The CMOS integration has also made device production much more affordable than its competitors.

SMO Sensor Fabrication

The highest complexity in the fabrication of an SMO sensor is the inclusion of a microheater. This requires thermal isolation from surrounding components, achieved with the formation of a suspended membrane, which uses air as a thermal insulator to the underlying silicon wafer, as shown in Figure 1. The most complicated part of the fabrication process is the formation of this membrane. There are two main methods for the membrane generation, one of which is the use of highly selective wet chemical etchants such as potassium hydroxide (KOH) or ethylenediamine pyrocatechol (EDP) (1); however, this technique is very expensive and low-cost alternatives are sought after. The low-cost option is the use of selective plasma etch processes, such as SF_6-based plasma chemistries, often used for silicon and silicon dioxide etching. The air isolation below the active area can also be achieved by etching to the membrane from the back of the wafer, meaning that no suspension beams are required. This method, although cheaper, has reduced power efficiency, since significant heat is lost by conduction through the entire membrane, a principal heat loss component in these structures. In suspended membranes, the conduction only takes place through thin suspension beams, as shown in Figure 1.

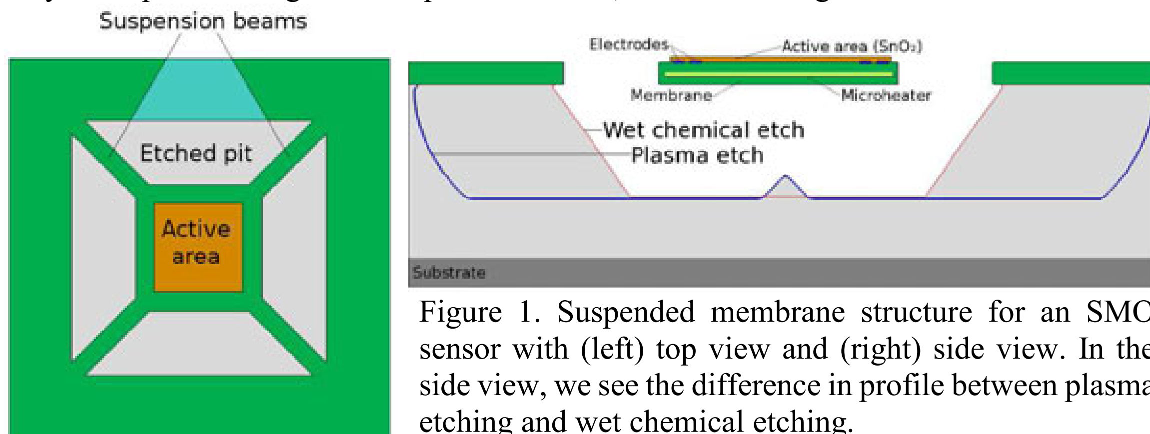

Figure 1. Suspended membrane structure for an SMO sensor with (left) top view and (right) side view. In the side view, we see the difference in profile between plasma etching and wet chemical etching.

More recently, STMicroelectronics has realized another method in generating the suspended porous membrane on a silicon wafer, based on a sacrificial polyimide (2). First, an isolating silicon dioxide is deposited using thermal oxidation or chemical vapor deposition (CVD). A sacrificial Polyimide HD8820 is subsequently spin-coated and selectively etched to form the sensor cavity, as shown in Figure 2. The membrane material is composed of a Tantalum-Aluminum (TaAl) micro-heater, sandwiched between two

silicon nitride (SiN) layers. SiN is deposited using low pressure chemical vapor deposition (LPCVD), while TaAl is patterned using physical vapor deposition (PVD) and subsequent plasma etching. The sensing material is deposited on top of the membrane, followed by the metal contacts (2). The applied sensing layer is tin dioxide (SnO_2), one of the most promising metal oxide materials for gas sensor applications. SnO_2 can be deposited using a variety of techniques: CVD, sputtering, pulsed-laser deposition, sol-gel process, and spray pyrolysis. The choice of sensing material is discussed in more detail in the following section.

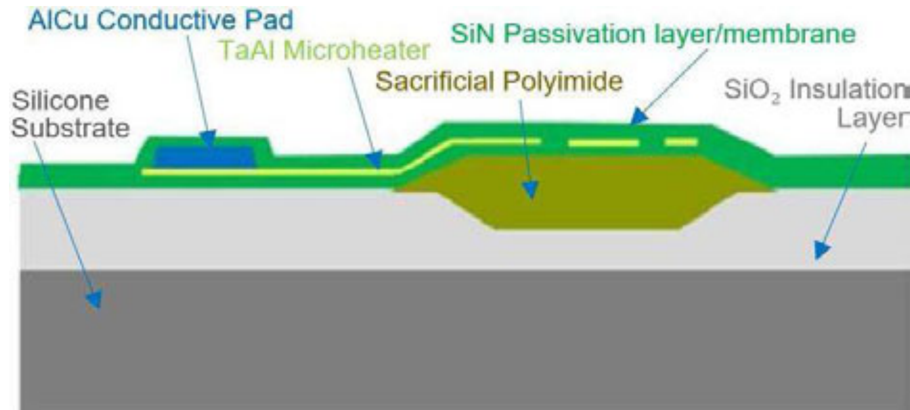

Figure 2. Two-dimensional cross-section cut through the material stack making up the microheater (2). The primary materials are shown, including the sacrificial Polyimide, which, when removed, forms the air cavity and the suspended membrane, ensuring thermal isolation between the microheater and the underlying silicon wafer.

Choice of Sensing Film

The miniaturization of transistors and other electronic devices has proven to be essential in advancing our technological capabilities. However, the chemical sensor field, until recently, lagged behind the overall progress of CMOS devices. Discoveries in the application of metal oxide semiconductors have narrowed this somewhat by enabling sensor miniaturization and integration with other electronics. Many SMOs have been extensively studied for their gas sensing properties, including indium oxide (In_2O_3), indium-tin-oxide (ITO), cadmium oxide (CdO), zinc tin oxide ($ZnSnO_4$), lead oxide (Nb_2O_5), and many more. Among the most promising, and those now beginning to enter commercialization, are tin oxide (SnO_2), zinc oxide (ZnO), and tungsten trioxide (WO_3). These three SMOs fulfill most, if not all, of the requirements for a good gas sensing performance, which is their sensitivity to a broad spectrum of potentially harmful gases, ease of deposition, and cost of fabrication.

The gas sensing capability of SnO_2 is well known and, over the last few years, it has become the most commonly used SMO for gas sensing, resulting in its commercialization. Figure 3 shows the response of an SnO_2 thin film to the presence of hydrogen (H_2) and carbon monoxide (CO) in the environment. The response to the presence of CO shown in the left plot in Figure 3 has been measured at 287°C for a sputtered film. The CO response shown in the plot on the right has been measured at 400°C for a spray deposited film, which also includes impurities in the form of platinum (Pt) nanoparticles (4). The presence of Pt impurities and the higher operating temperature results in an increase in the sensing performance by almost ten times. The symbols in the figure represent measured data while the solid lines are best-fit lines, discussed in more detail in (5).

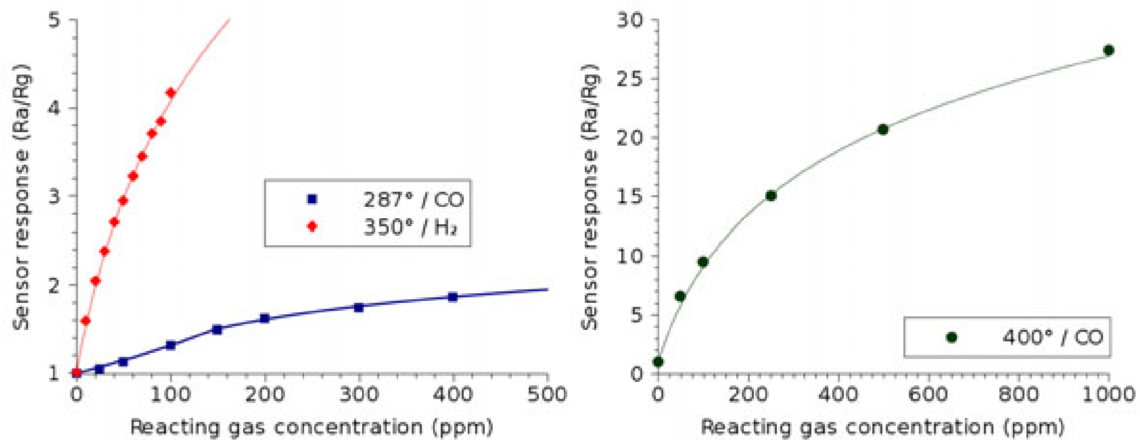

Figure 3. SnO_2 thin film sensor response during exposure to a varying concentration of carbon monoxide (CO) and hydrogen (H_2) gas. The temperatures used during the measurements correspond to the optimal temperature of operation for the detection of the target gas. Ra and Rg are the film resistances in air and in the presence of a target gas.

Microheater Design

Many attempts have been made over the years to optimize the geometry of the heater in order to achieve temperature uniformity in the active membrane region. Several designs involve the placement of a highly thermally conductive element (silicon, polysilicon, or metal) below or above the microheater in order to distribute the heat more uniformly. A more widely used approach is using efficient designs for the microheater geometry. The geometries can be broadly classified as rectangular, square, circular, or irregular, further subdivided into honeycomb, drive wheel, elliptical, etc. shown in Figure 4 (6). The meander design, shown in Figure 5, is most commonly used in combination with rectangular or circular geometries. The line widths and the separation between lines has a significant influence on the efficiency of the temperature distribution.

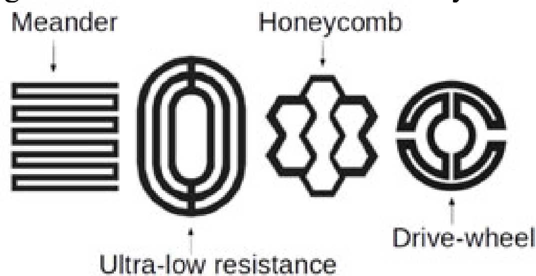

Figure 4. Studied microheater designs, including meander, elliptical, honeycomb, and drive wheel.

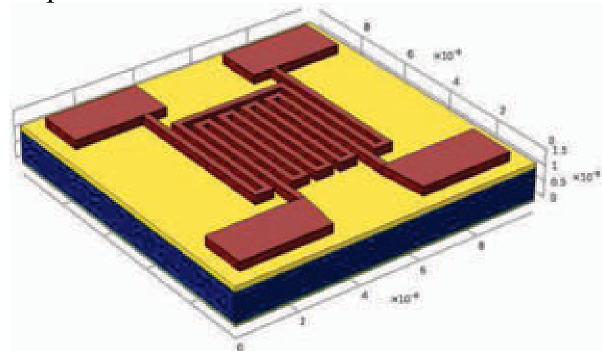

Figure 5. Meander microheater design with a square pattern. The second line is used for temperature measurements.

Extensive work has been done recently on novel microheater designs to improve the temperature uniformity, power consumption, and thermal isolation, while easing the fabrication requirements. The designs achieved in (3) have a membrane area of 0.9mm × 0.6mm, with a structural membrane stack formed with layers of 500nm thick silicon dioxide (SiO_2), 300nm thick silicon nitride (Si_3N_4), and an additional 500nm thick SiO_2. Platinum was used for the microheater and electrodes for its stability, linearity, and

resistance to oxidation at a broad range of operating temperatures. Aluminum-copper (AlCu) is chosen for the microheater pads for its high electrical conductivity and thermal conductivity lower than gold. For electrical insulation between microheater and sensor contact metallization, a 300nm thick silicon dioxide layer is deposited on top of the microheater. The two recently suggested novel geometries, which address key concerns for gas sensor developers are: microheater array design and dual hotplate design. A short description of the designs will be given here, while an in-depth analysis is provided in Lahlalia et al. (3).

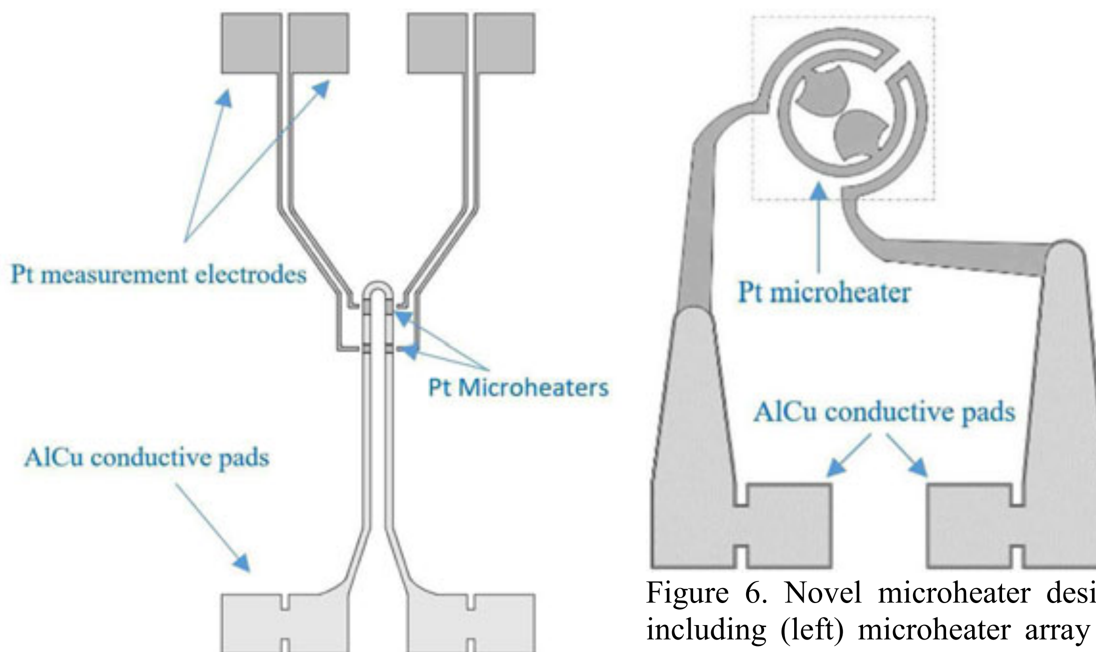

Figure 6. Novel microheater designs, including (left) microheater array and (right) dual hotplate geometries.

Microheater Array

The microheater array is shown in Figure 6 (left) and combines small resistances in an array instead of a conventional single-layer microheater. This provides localized heating of the sensing layers to different temperateness at different locations, thereby allowing for a natural integration of a sensor array using a single heat source and at reduced power dissipation. The small hotplate resistances also provide an ultra-fast thermal response time, enabling the microheater to operate in ultra-short pulse mode, further reducing the average power consumption to a few hundred μW.

Since the sensitivity of the SMO films towards target gases is optimal only at a single temperature, as depicted in Figure 7, the array can be used to simultaneously detect reactions at multiple temperatures. Here, we see the sensitivity of doped and undoped SnO_2 thin films in detecting methane (CH_4), H_2, CO, and propane (C_3H_8). The collected measurements can subsequently be processed and treated using non-parametric analysis such as principal component analysis, discriminant functions, or neural networks to distinguish between each gas, improving the overall selectivity of the SMO sensor, while not harming its sensitivity (8)(9). Recently, an additional improvement on this integration was suggested by introducing two sensing layers, deposited within the same membrane structure (3). The design allows for further capabilities in adjusting the microheater dimensions and position in order to incorporate even more sensing layers, effectively solving the problem of selectivity in SMO gas sensors altogether. With this design, we also

noticed a reduction in current crowding by about 20%, when compared to conventional designs, thanks to the slopes added at the extremities of each conductive pad. The sensitivity is measured as the ratio of the resistance reduction in the presence of a target gas, when compared to the resistance in air or inert ambient, given by:

$$\text{Sensitivity} = (R_{air} - R_{gas}) / R_{air}, \quad [1]$$

where R_{air} represents the baseline resistance after stabilization in ambient and R_{gas} is the resistance of the sensitive layer after exposure to a target gas.

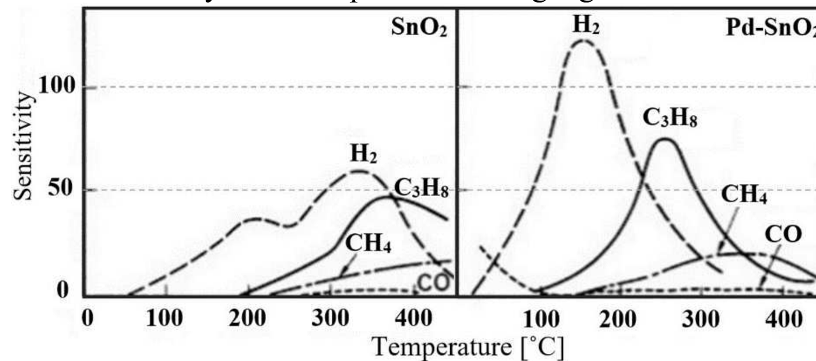

Figure 7. Sensitivity of doped and undoped SnO_2 towards different gases as a function of operating temperature (7). The concentrations of gases are 0.5%CH_4, 0.8%H_2, 0.02%CO, and 0.2%C_3H_8. It is evident that a multi-temperature sensor can provide added selectivity.

Dual-Hotplate

The dual-hotplate design is shown in Figure 6 (right) and is a combination of a single circular microheater, suggested by Elmi et al. (10), together with two passive micro-hotplates, suggested by Lahlalia et al. (3). The hotplates are used for improved thermal uniformity in the active region. Even a minor variation in the temperature over the sensing element can lead to baseline drift, changing the baseline resistivity of the SMO sensor, thereby requiring additional electronics for frequent calibrations. The fact that the additional hotplates are electrically passive ensures that the power consumption is kept at a minimum, which is also a critical factor to improve the stability of the sensor baseline.

A new membrane shape has been designed to accompany the dual-hotplate structure, formed by four curved micro-bridges, in order to provide improved insulation against heat losses to the substrate, shown in Figure 8 (right). In Figure 8 (left) the three-armed membrane shape, used with the microheater array, is shown. The differences in the mechanical stability of the two membrane types are discussed in the following section.

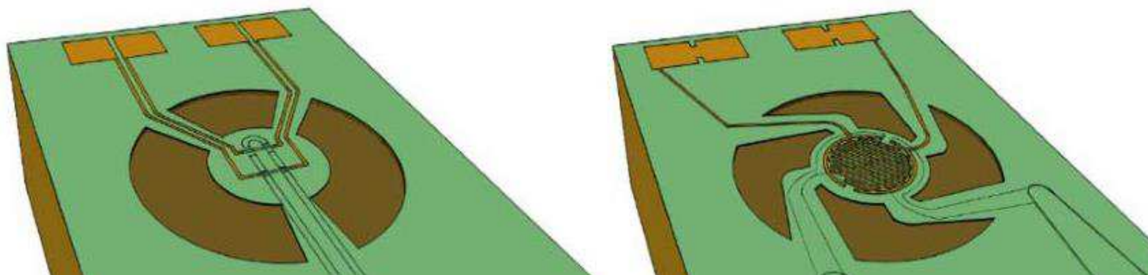

Figure 8. SMO gas sensor membranes designs, used with the (left) microheater array and (right) dual-hotplate. The inner circular membrane has a diameter of 180µm, while the membrane hole has a diameter of about 400µm.

Modeling and Analysis of SMO Sensor Structures

In order to have a complete picture of the fabrication, reliability, and operation of SMO gas sensors, measurements alone do not suffice. Many modeling techniques and simulation tools are essential in order to provide an in-depth analysis of the interplay between different materials in this complex structure. In this section the essential modeling approaches used to gain a deeper understanding of SMO gas sensors are described. These include the fabrication of the CMOS-integrable devices, electro-thermal modeling using finite element methods (FEM) and compact models, mechanical simulations using FEM, and modeling of the sensing film conductivity. With regard to the microheater operation, the focus is on its power dissipation, thermo-mechanical properties, and mechanical stability (11), while the SnO_2 metal oxide is discussed in terms of its conductive response to the presence of various gases in the environment (4).

SMO Sensor Fabrication Techniques

The complexity in the fabrication of SMO gas sensor devices is heightened due to the need for a thermally-isolated membrane. As mentioned earlier, this membrane can be generated by etching from the back of the wafer using deep reactive ion etching (DRIE) techniques or from the top, through openings in the membrane using wet chemical etching or plasma etching. When etching from the back, a closed membrane is generated, while etching through holes results in a suspended membrane with suspension beams connecting the active region to the rest of the structure (12). The closed membrane thicknesses are in the range between 1µm and 2µm, but the required back-side etching techniques make the process more expensive and not fully CMOS-compatible (13). For this reason, we concentrate our studies on the suspended-membrane sensor.

A thorough analysis has been performed on a typical geometry with an active area of 100µm × 100µm using both wet chemical potassium hydroxide (KOH) and SF_6 plasma models (14). The simulation for KOH etching was achieved using the model described in (15) and the ViennaTS tool (16). Using a 150 minute etch with a KOH concentration of 30% and a temperature of 70°C, the suspended membrane was generated with a 100µm hole. The silicon etch rate is dependent on the crystallographic orientation and, under the noted etch conditions, the rates for directions <100>, <110>, <111>, and <311> were found to be R_{100}=13.3nm/s, R_{110}=24.2nm/s, R_{111}=0.1nm/s, and R_{311}=23.9nm/s, respectively. Although the KOH structure displays a very clean geometry without undesirable lateral etching (Figure 1), the process can be very corrosive to the surrounding devices. For this reason, further analyses of the plasma etching on the same geometry have been carried out. This process is less corrosive and more compatible with CMOS fabrication, but suffers from profound lateral etching, as shown in Figure 1.

Simulations of plasma etching are carried out using the physics described by the group at the University of California in (17) and (18), implemented within the ViennaTS tool (16). The key idea is to use a stochastic approach to the particles, which are present in the plasma chamber and which have an influence on the etching process. The particles can either be neutral, representing a chemical etch component, or ionic, representing a physical etch component. The chemical etch component is the primary contributor to the lateral etching underneath the eventual suspended membrane. However, since the lateral etching proceeds in all directions, the overall size required by the sensor increases when this method is

applied. Using SF_6 plasma chemistry with a fluorine flux of $1\times10^{19}cm^{-2}s^{-1}$ and disregarding any ion involvement, a 300 second etch was sufficient to expose the membrane to the level shown in Figure 1. In follow-up analysis, we found that the lateral etching had no adverse effects on the stress distribution in the active sensor region (14).

Another aspect of the sensor fabrication which has been investigated is the deposition of the sensing SMO film itself. This layer can be deposited in a variety of ways, including chemical vapor deposition, sputtering, pulsed-layer deposition, sol-gel process, rheotaxial growth and vacuum oxidation, and spray pyrolysis (14). Sputtering and spray pyrolysis are methods which are quite straight forward and cost effective to implement within the CMOS sequence. Using both etching methods, the resulting geometry was analyzed with ViennaTS (16). Spray pyrolysis showed a more isotropic coverage around corners and edges; however, the spray pyrolysis deposition requires elevated temperatures (400°C), meaning that a thermal stress can develop in the film due to the subsequent cooling to room temperature. This is not necessarily a disadvantage, since it results in having a film which is relatively stress-free at elevated temperatures. Considering that the SMO film must be heated to temperatures in the range of 250°C to 500°C in order to activate sensing, this may in fact be an advantage for the mechanical stability of the device.

Electro-Thermal Analysis

Modeling the electro-thermal behavior of the sensor and microheater in particular is essential to understand the heat losses, shown in Figure 9, and thereby to minimize the power dissipation in the design. The analysis is usually performed in a finite element environment, which requires meshing the full geometry followed by memory and computationally intensive simulations. The ambient conditions in the model are set to room temperature (20°C) and the heat transfer coefficient is temperature dependent and ranges from about $90W/m^2K$ at 100°C to $125W/m^2K$ at 400°C, as reported in (3).

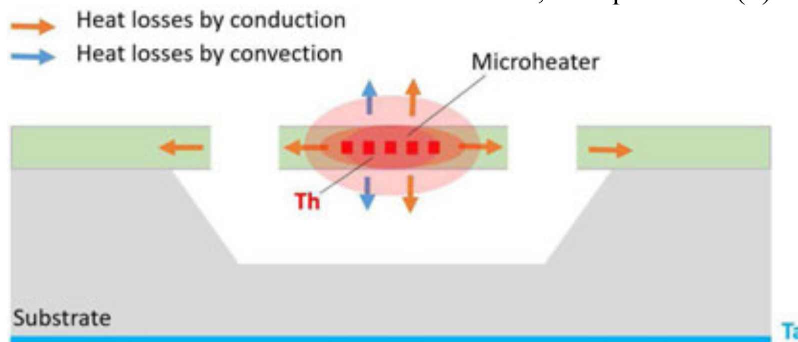

Figure 9. Heat loss mechanisms in the SMO gas sensor and surroundings, where T_h is the microheater temperature, required for sensor operation and T_a is the ambient temperature.

The main sources of heat loss, depicted in Figure 9 are conduction and convection through the air and conduction through the membrane. There is a slight loss to radiation in the air, but this is relatively minor when compared to other losses. In (19) we calculated the heat conduction for a typical 100µm × 100µm sensor structure, which required a total of 32.5mW to heat at 400°C. Of the total dissipated 32.5mW, 18.9mW was lost to the air conduction above the membrane and 1.3mW to the air conduction below the membrane. About 12.2mW was lost to the conduction through the membrane beams, while a minimal 0.16mW was lost to radiation. Therefore, we can safely conclude that the bulk of the heat lost is through the membrane and air conduction through the top.

With this in mind, the microheater array and dual-hotplate designs, presented in the previous section, were optimized and significantly improved, resulting in a total power dissipation of only 9.31mW and 8mW, respectively, when operating at 350°C (3). In Figure 10, the thermal distribution for the two designs is shown. Here, we also note that the temperature uniformity across the active region is very good, with total variations below 10°C or below 3%. In the microheater array design on the right of Figure 10 we also see two active regions with two different target temperatures operating simultaneously. This design allows us to heat the sensor to 270°C and 350°C at the same time, meaning that we can selectively test for C_3H_8 and CH_4 (Figure 7) during a single current pulse.

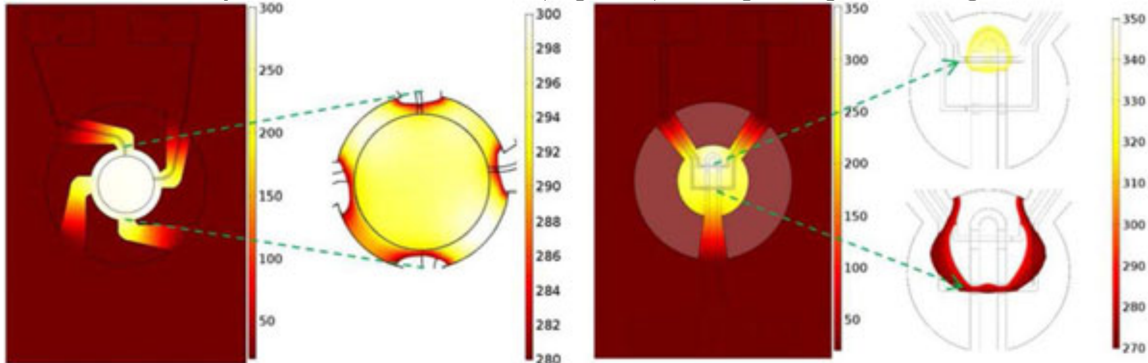

Figure 10. Simulation of the thermal distribution (°C) in a (left) dual-hotplate design and (right) a microheater array design. The microheater array allows for concurrent operation at multiple temperatures.

To eliminate the need for FEM simulations and the associated meshing and computational requirements, an analytical compact model has been developed, which can be used to calculate the electro-thermal behavior of the sensor (3). The model emulates an integrated circuit (IC) using thermal elements, represented using an electrical circuit equivalent. In Table I the relationship between the metal's thermal properties and an electrical component equivalent is shown. Using this strategy, the complete sensor geometry is discretized and an IC, which is capable of very accurate calculations of the heat loss by convention, is generated.

TABLE I. Parameters for a thermal model equivalent of an electrical circuit model.

Thermal parameter	Electrical equivalent	Thermal parameter	Electrical equivalent
Temperature (K)	Voltage (V)	Heat flow (W)	Current (A)
Specific heat (J/Kg·K)	Permittivity (F/m)	Thermal conductivity (W/K·m)	Electric conductivity (S/m)
Thermal resistivity (K·m/W)	Electric resistivity (Ω·m)	Heat (W.s)	Charge (A·s)
Thermal resistance (K/W)	Electric resistance (Ω)	Thermal capacitance (W.s/K)	Electric capacitance (F)

Mechanical Reliability Analysis

One of the major concerns regarding the lifetime of SMO gas sensors is the stability of the suspended membrane. The high temperatures, combined with a variety of materials with different coefficients of thermal expansion (CTE), can lead to the build-up of excessive stress in the membrane and eventual cracking or delamination failures. The stress

in the membrane is a combination of the residual stresses in the layers which make up the complete membrane stack. This stress builds up due to two factors: intrinsic stress during film growth and grain formation and thermal stress, present due to the post-deposition cooling to room temperature. The deposition of metal and semiconductor layers most often follows the Volmer-Weber growth mode, which involves the generation of islands, which then grow and impinge on each other, forming grains and grain boundaries (20). We have studied this type of stress build-up in the membrane layers as well as in the SMO film itself (21), showing that spray pyrolysis deposited films suffer from a higher stress at room temperature than sputtered films. However, during operation at elevated temperatures, the sputtered films experience increased thermal stresses.

Using FEM, the effects of the stress on the deformation in the membrane layer have been studied. Surprisingly, we have found that the stress distribution in the active area is unaffected by the method of the membrane formation, whether using KOH or plasma etching (14). However, the maximum displacement, at the center of the membrane (with a 100μm × 100μm active region), was found to be 8μm for the plasma-etched membrane, compared to 5μm for the KOH-etched membrane. This is due to the effective expansion in the membrane width due to the lateral etching component during plasma etching. The displacement in the novel suspended membrane structures for the microheater array and dual-hotplate designs, when heated from 20°C to 300°C, are shown in Figure 11. We note a displacement of about 3μm for the 4-beam design and about 0.8μm for the 3-beam design. This means that the designs both improve upon the generic membrane structure from Figure 1 and that the 3-beam membrane displaces much less, indicating that it has a reduced likelihood of crack formation on the surface of the sensing element.

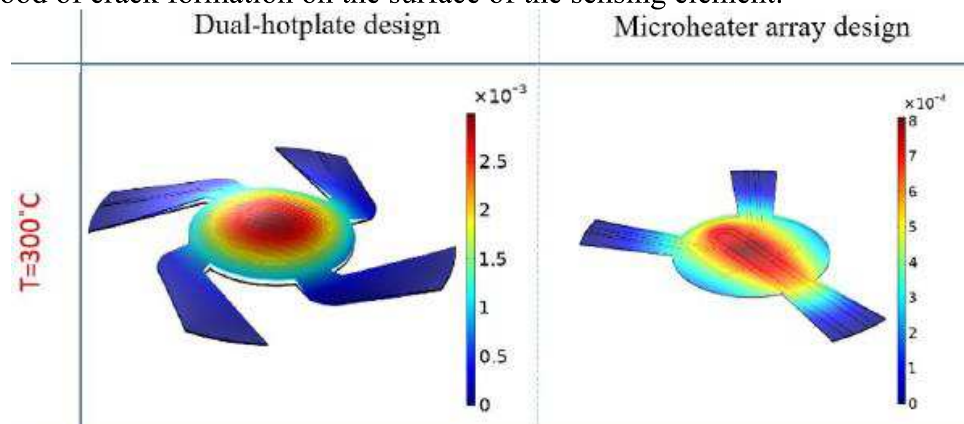

Figure 11. Total displacement (mm) of the membrane stack when heated from room temperature (20°C) to 300°C.

Characterization of the SMO Film

A complete understanding of the operation of the SMO sensor is not yet available, but significant progress has been made recently in understanding conductivity in one of the most frequently used SMOs, SnO_2. The electrical conduction of the n-type SnO_2 film is modeled using drift-diffusion equations, where only electrons, the majority carriers, are considered (22). The electron concentration and the mobility vary significantly with temperature, even in a fully inert environment (23); therefore, also the conductivity is significantly influenced by temperature, as depicted in Figure 12. When a potential is applied across the film, the electric field is derived from the solution to the Poisson equation, with boundary conditions which relate the surface charge density to an applied electrical

potential. This is not unlike a transistor; however, instead of directly applying a potential at the gate, a potential is applied indirectly through the accumulation of charges at the surface. This charge stems from the ionosorption of gases at the SMO surface.

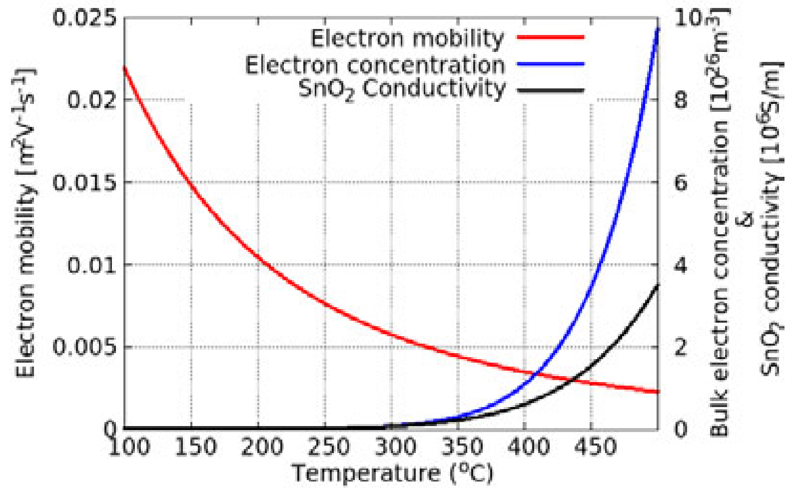

Figure 12. Temperature dependence on the electron concentration (n_e) and mobility (μ_e) of SnO_2. The conductivity is a combination of both n_e and μ_e by $\sigma = q \cdot \mu_e \cdot n_e$.

The surface potential V_s is solved for by using the Schottky relation

$$V_s = - (q \cdot N_{eff}^2) / (2 \cdot \epsilon \cdot N_D), \quad [2]$$

where N_D is the donor density, ϵ is the permittivity of SnO_2, q is the electron charge, and N_{eff} is the sum of the electrons which gain enough power to reach the surface and the external electrons donated from adsorbed or ionosorped gas ions (24). The ionosorption of gas molecules attracts electrons from the SnO_2 bulk, resulting in band-bending at the interface between the material and the surrounding gas. The amount of band bending is proportional to the effective concentration of localized surface electrons N_{eff} (22). In Figure 13, the surface charge density is plotted versus time at various temperatures in a synthetic air environment, where O^- and O^{2-} ions are adsorbed at the surface.

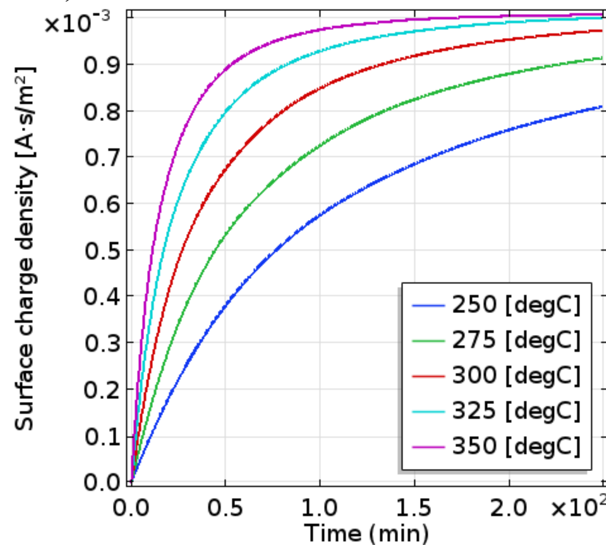

Figure 13. Surface charge density [A·s/m^2] in a synthetic air environment, with 80% N_2 and 20% O_2. This shows the effects of the surface ionosorption with O^- and O^{2-} ions.

Conclusion

Advanced modeling and simulation tools have been used to obtain a deeper understanding of the fabrication, reliability, and operation of semiconductor metal oxide gas sensor. The advanced analysis and characterization have allowed us to develop optimized sensor designs which reduce the power consumption, improve temperature uniformity, and minimize stress accumulation. When characterizing the fabrication of SMO sensors, the essential processes are the etching step for the creation of a suspended membrane and the deposition of the sensing film itself. Both processing steps were analyzed using the ViennaTS tool at the Institute for Microelectronics, TU Wien. For mechanical simulations, in order to understand the stress build-up and distribution in the complex structure, finite element analysis have been carried out. Electro-thermal characterization has been performed using FEM and a compact model has been developed as a means to represent the thermal behavior of the sensor in an equivalent electrical circuit form. Finally, calculations have been performed in order to characterize the effects of gas ionosorption at the surface of SMO thin films. The adsorbed charges generate an effective surface potential, which forms an electric field, influencing the behavior of the charge carriers in the SMO and thereby also its conductance.

References

1. P. Bhattacharyya, *IEEE Tran. Dev. Mat. Reliab.* **14**(2), pp. 589-599 (2014).
2. R. Shankar et al., Patent publication number US20160018356 A1 (2016).
3. A. Lahlalia, L. Filipovic, and S. Selberherr, *IEEE Sensors J.* **18**(5), pp. 1960-1970 (2018).
4. L. Mädler et al., *J. Nanopart. Res.* **8**(6), pp. 783-796 (2006).
5. L. Filipovic and S. Selberherr, *Sensors* **15**(4), pp. 1843-1848 (2015).
6. S.M. Lee et al., *Microelectron. J.* **34**(2), pp. 115-126 (2003).
7. N. Yamazoe and N. Miura, *Chem. Sensor Technol.* **4**, pp. 19-42 (1992).
8. S. Banerjee, A. Dan, and D. Chakravorty, *J. Mater. Sci.* **37**(20), pp. 4261-4271 (2002).
9. Y. Cui et al., *Science* **293**(5533), pp. 1289-1292 (2001).
10. I. Elmi et al., *Sens. Actuators B, Chem.* **135**(1), pp. 342-351 (2008).
11. L. Filipovic and S. Selberherr, *IEEE Trans. Device Mater. Rel.* **16**(4), pp. 483-495 (2016).
12. I. Simon et al., *Sens. Actuators B, Chem.* **73**(1), pp. 1-26 (2001).
13. A. Götz et al., *Sens. Actuators B, Chem.* **44**(1), pp. 483-487 (1997).
14. L. Filipovic and S. Selberherr, in *Proc. TENCON 2015*, pp. 1-6 (2015).
15. B. Radjenović and M. Radmilović-Radjenović, *Thin Solid Films* **517**(14), pp. 4233-4237 (2009).
16. ViennaTS, The Vienna Topography Simulator online: http://www.iue.tuwien.ac.at/software/software/viennats/.
17. S. Gomez et al., *J. Vac. Sci. Technol., B* **22**, pp. 606-615 (2004).
18. R.J. Belen et al., *J. Vac. Sci. Technol.*, A **23**(1), pp. 99-113 (2005).
19. L. Filipovic and S. Selberherr, *Microelectron. Rel.* **61**, pp. 3-10 (2016).
20. S.C. Seel, PhD Dissertation, Massachusetts Institute of Technology (2002).
21. L. Filipovic and S. Selberherr, *ECS Transactions* **66**(5), pp. 243-250 (2015).
22. G. Tulzer et al., *Nanotechnol.* **24**(31), pp. 315501(10) (2013).
23. A. Fort et al., *Sens. Actuators B, Chem.* **124**(1), pp. 245-259 (2007).
24. N. Barsan et al., *Sens. Actuators B, Chem.* **207**(A), pp. 455-459 (2015).